SIMULATION AND ANALYSIS OF AIRBORNE LIDAR BATHYMETRY ON CAPILLARY-GRAVITY WATER SURFACE DETECTION

Chih-Kai Meng[1*] and Jen-Jer Jaw[2]
[1] Master, Department of Civil Engineering, National Taiwan University,
No. 1, Sec. 4, Roosevelt Road, Taipei, 10617 Taiwan, +886-2-23678645;
E-mail: r98521110@ntu.edu.tw

[2] Associate Professor, Department of Civil Engineering, National Taiwan University,
No. 1, Sec. 4, Roosevelt Road, Taipei, 10617 Taiwan, +886-2-23678645;
E-mail:jejaw@ntu.edu.tw

KEY WORDS: Airborne LiDAR bathymetry, water surface, capillary-gravity wave facets, waveform, timing estimator

ABSTRACT: Airborne LiDAR bathymetry has been proven an ideal technique in both safety and efficiency concerns for 3-D topographic surveying in both shallow water and tidal flat areas. Yet the crucial challenge for acquiring terrain of water bottom is to precisely capture the trajectory of laser pulse when travelling between different medium, air and water. Therefore, the quality of mapping 3-D bottom terrain would depend on how well the waveform analysis on determining the timing hitting water surface and water bottom can be designated. The goal of this research is to comprehend the reaction of laser pulse on water surface, mainly wind- induced capillary-gravity wave facets. In particular, laser scanning geometry and the meteorological factor that shape the waveform geometrically and radiometrically are analyzed and thus the better timing detection method can be advised. In additional to gaining better understanding of laser-to-water interaction, this work may contribute to highlighting the significance of water surface detection which current airborne LiDAR bathymetric systems overlook.

1. INTRODUCTION

For the purpose of national defense and people's quality of life, the government has been working on the mapping of the 3D topographic terrain in coastal waters near Taiwan and Ponghu. The ship-based SoNAR, a commonly-used sensor for seabed terrain mapping, may touch the bottom of the tidal flat. The Airborne LiDAR Bathymetry(ALB), however, owns the advantages of both safety and efficiency.
In academic field, the return information about data retrieved from ALB is divided into three categories: interface return, water column return, and bottom return. In order to get the precise 3D terrain information, the traveling path of a single laser pulse must be fully comprehended. Therefore, the timing of interface return and the timing of bottom return are especially important. However, current studies on the interface return and the timing of the laser pulse reaching the interface are relatively less, which give rise to less reliability of the mapping results.
In order to understand the properties of interface return and the precise reaching time of the laser pulse, the research will be based on a wind-induced capillary-gravity wave model. By simulating the ALB's laser pulse and tracking the laser's trajectory, the research can show the range of the different parameters like wind speed and the scanning angle may affect the waveform.

2. METHODOLOGY

The methodology includes water surface model, optical correlation, and timing estimator.

2.1 Water Surface Model

2.1.1 Sea Water Movement There are three types of sea water movement: (1). Ocean current, (2). Tide, (3). Wave. The major causes of ocean current are external forces which include Coriolis Force, universal gravitation, planetary wind system, local wind system, and density current. Tide is sea level that moves up and down periodically, and it can be classified into two groups: astronomical tide and meteorological tide. Wave is the result of wind, and is categorized into capillary wave and gravity wave. The former's period is shorter, whereas the latter's is longer(Chu, 2011).
The last paragraph mentions the different scale of sea water movement. However, the ALB laser pulse's contact with the interface is locally correlated. The small part of the wave changes is the major causes of the return signals. Based on this, the research will use the wind-induced capillary-gravity wave as the interface model(Mobley, 2002；Tulldahl and Steinvall, 2004).

2.1.2 Capillary-Gravity Wave Facets Mobley(2002) considered a wind blowing across a water surface and momentarily maintaining a set of capillary waves. The water surface elevation η changes erratically in time because of the passing waves(see Figure 1).

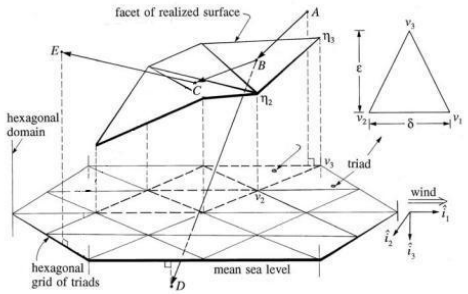

Figure 1. Model of the water surface as a hexagonal grid of triangular wave facets. (Mobley, 2002)

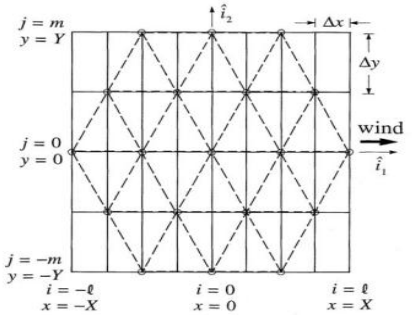

Figure 2. Gravity random water surface (Mobley, 2002)

In contrast to capillary waves, the period of gravity waves is longer. Moreover, the nodes of the gravity waves are based on wind speed and gravity(see Figure 2). The details about the above mentioned are described in Meng(2011).

2.2 Monte Carlo Simulation

Law and Kelton(1991) mentioned "We define Monte Carlo simulation to be a scheme employing random numbers, that is, U(0,1) random variates, which is used for solving certain stochastic or deterministic problems. "
This research is based on Monte Carlo simulation to simulate the photons of each laser pulse.

2.3 Optical Correlation

2.3.1 Refraction And Reflection The research focuses on the optical correlation of the water interface, which mainly concerns refraction and reflection(see Figure 3).

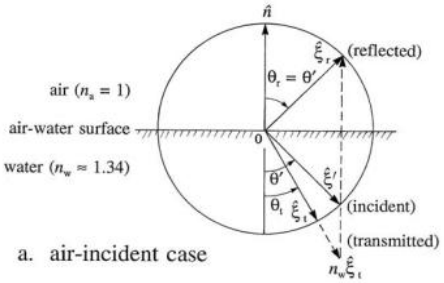

Figure 3. Air incident case(Mobley, 2002)

In the air-incident case shown in Figure 3, a ray of photons approaches the air-water surface along direction $\hat{\xi}'$, $\hat{n}$ is a unit vector normal to the surface. Upon reaching the water surface, the ray $\hat{\xi}'$ produces two daughter rays: a reflected ray along $\hat{\xi}_r$ and a transmitted (refracted) ray along $\hat{\xi}_t$. The directions $\hat{\xi}_r$ and $\hat{\xi}_t$ lie in the plane defined by $\hat{\xi}'$ and $\hat{n}$. One can compute the directions $\hat{\xi}_r$ and $\hat{\xi}_t$ by observing the coplanarity of the vector tips of the reflected direction and the modified transmitted or incident directions. This coplanarity, which is shown by the dashed lines in Figure 3, follows from Snell's law written for the air-incident case:

$$\sin\theta' = n_w \sin\theta_t \tag{1}$$

And the reflected vector $\hat{\xi}_r$ can be calculated by equation(2)

$$\hat{\xi}_r = \hat{\xi}' - 2(\hat{\xi}' \cdot \hat{n})\hat{n} \tag{2}$$

2.3.2 Fresnel Reflectance Equation (3) shows that the Fresnel reflectance is used to calculate energy remained after contact with certain plane. If number of reflection time increases, the energy remained will be less.

$$r(\theta') \equiv r(\hat{\xi}' \cdot \hat{n}) = \frac{1}{2}\left\{\left[\frac{\sin(\theta' - \theta_t)}{\sin(\theta' + \theta_t)}\right]^2 + \left[\frac{\tan(\theta' - \theta_t)}{\tan(\theta' + \theta_t)}\right]^2\right\} \tag{3}$$

2.4 Ray Tracing Algorithm

The ray tracing includes finding the laser pulse's contact point with the wave facets, the photon's geometry in the water surface model, and the receiving numbers and energy of photons(the minimal unit of laser pulse).

2.5 Waveform Timing Estimator

The return pulse's timing estimators are as follows: maximum slope change, center of area(COA), mean, peak, midpoint, and 50% risetime point(see Figure 4).

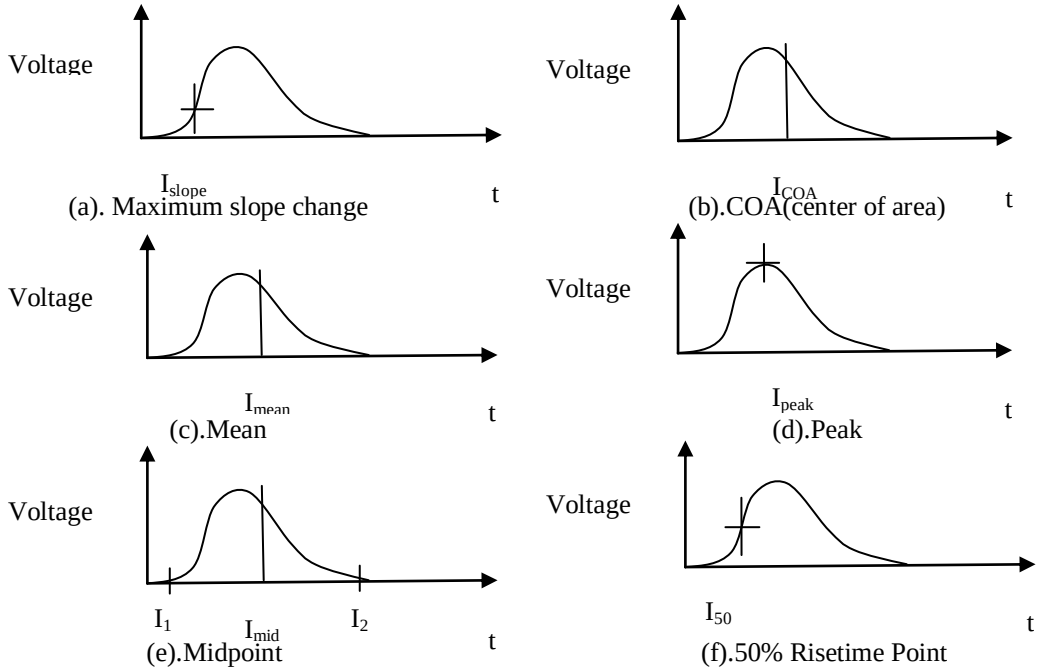

Figure 4. Timing estimators(Abshire, 1994)

3. EXPERIMENT ALIGNMENT

In order to simulate the correlation between photons and the water surface, the experiment alignments initially build the water surface model according to the wind speed, and then followed by location set up of ALB. Lastly Monte Carlo simulation is used to produce waveforms.

3.1 Waveform Experiment Alignment

According to the ALB system which is in operation now, the parameters of the laser pulse generator are as follows(see Table 1):

Table 1. Alignment of laser pulse generator

Laser Power(mjoule)	5
Photon Numbers	1000000
Pulse Width(ns)	7
Pulse Resolution(ns)	0.01
Wave Length(nm)	532
Height(m)	400
Source Diameter(mm)	100
Source FOV(mili-radian)	5
Sensor Diameter(mm)	100
Sensor FOV(mili-radian)	21
Viewing Angle(degree)	20

3.2 Circular Disk And Photons

Shown in Figure 5, the light source is modeled as a circular disk. The photon starts from the location with radius of ρ_s and azimuth angle of θ_s. Assuming that the energy distribution at the laser is uniform, the ratio of A_s and A_l is a constant(see equation(4)).

$$\frac{A_s}{A_l} = \frac{\pi \rho_s^{\,2}}{\pi \rho_l^{\,2}} = \Lambda_1 \tag{4}$$

After the arrangement, the radius is shown in equation(5).

$$\rho_s = \rho_l \sqrt{\Lambda_1} \tag{5}$$

And, the azimuth angle is shown in equation(6).

$$\theta_s = 2\pi\Lambda_2 \tag{6}$$

Λ_1 and Λ_2 are iid U(0,1).

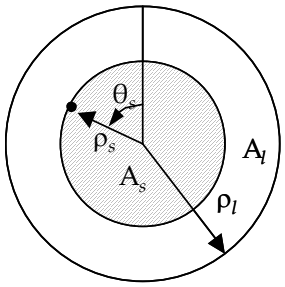

Figure 5. Circular disk
(Wang *et al.*, 2011)

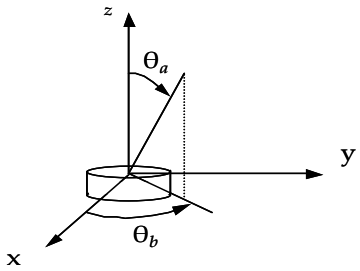

Figure 6. Photon direction exiting the light source
(Wang *et al.*, 2011)

3.3 Photon Direction

The photon's firing direction is shown in Figure 6. Now it is assumed that the photon density is uniform across the transmitter aperture. The area of the hemisphere covered by the scattering angle θ_a is proportional to that covered by the half FOV of the transmitter (see equation(7)).

$$\frac{2\pi \int_0^{\theta_a} \sin\theta d\theta}{2\pi \int_0^{FOV/2} \sin\theta d\theta} = \Lambda_3 \tag{7}$$

After arrangement, θ_a is shown in equation(8).

$$\theta_a = \arccos\theta\left[1 + \Lambda_3(\cos(\frac{FOV}{2}) - 1)\right] \tag{8}$$

And, the azimuth angle is shown in equation(9).

$$\theta_b = 2\pi\Lambda_4 \tag{9}$$

Λ_3 and Λ_4 are iid U(0,1).

3.3 Wind Speed Alignment

The research will use gentle breeze(5m/s), cool breeze(10m/s), and fresh gale(20m/s) as the wind speed alignment(Center Weather Bureau, 2011). The differences between each wind speed are shown from Figure 7 to Figure 9.

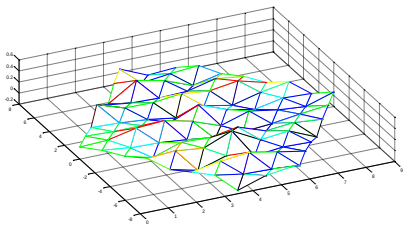

Figure 7. Gentle breeze on capillary-gravity wave
(unit: cm)

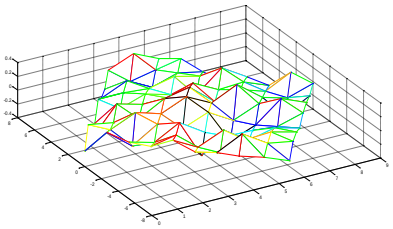

Figure 8. Cool breeze on capillary-gravity wave
(unit: cm)

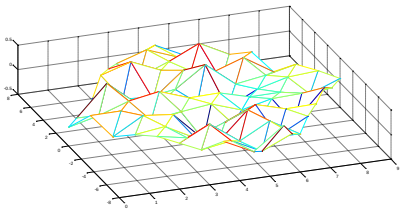

Figure 9. Fresh gale on capillary-gravity wave
(unit: cm)

Under the condition of gentle breeze, the maximum amplitude of the wave is about 0.1 cm. As for larger wind speed, the maximum amplitude of the wave can be up to 0.3 to 0.5 cm.

4. EXPERIMENT RESULT

4.1 Waveform Experiment – Different Wind Speed's Effects On Waveform And Timing Estimator

Under height 400 m and viewing angle 20 degree, the waveform results of 5m/s, 10m/s, and 20m/s wind speed are shown in Figure 10. The timing of maximum amplitude is near 2.84*10^-6 seconds. Changing different wind speed may cause different amplitude of water surface. However, under Monte Carlo simulation, the result shows that the returning photons are mostly only from one reflection during the period(Meng, 2011). Results of different timing estimator are shown in Table 3.

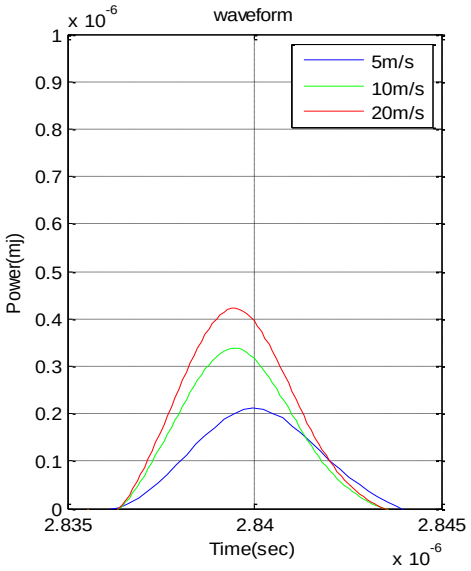

Figure 10. Waveform under different wind speed

Table 2. Results of timing estimators

	Wind speed:5m/s		Wind speed:10m/s		Wind speed:20m/s	
Timing estimators	**second** *10^-6	**Height(m)**	**second** *10^-6	**Height (m)**	**second** *10^-6	**Height (m)**
Maximum slope	2.8377	399.983	2.8377	399.980	2.8377	399.975
50% Risetime Pt.	2.8380	400.026	2.8380	400.015	2.8380	400.008
COA	2.8397	400.260	2.8397	400.259	2.8397	400.255
Mean	2.8395	400.237	2.8395	400.233	2.8395	400.232
Midpoint	2.8405	400.379	2.8405	400.379	2.8405	400.379
Peak	2.8398	400.280	2.8398	400.279	2.8398	400.277

It can be shown from Table 2 that in low wind speed, the maximum slope change can be the better choice. As for lager speed, the 50% Risetime Point is ideal for estimating time. And the maximum distance between timing estimators is 40 cm.

4.2 Waveform Experiment – Different Viewing Angle's Effects On Waveform

According to the ALB's system parameters, the research will use viewing angle 10, 15, and 20 for simulation.

4.2.1 Low Wind Speed The results are shown in Figure 11. Under low wind speed and small viewing angle, the photons are tend to retract back to the sensor, resulting in larger amplitude of waveform.

4.2.2 High Wind Speed Under high wind speed, the amplitude of water surface will be larger. Along with small viewing angle, the geometry will cause small amplitude of waveform. Figure 12 shows the amplitude of waveform is proportional to the viewing angle, and this is inversely proportional to the case in low wind speed.

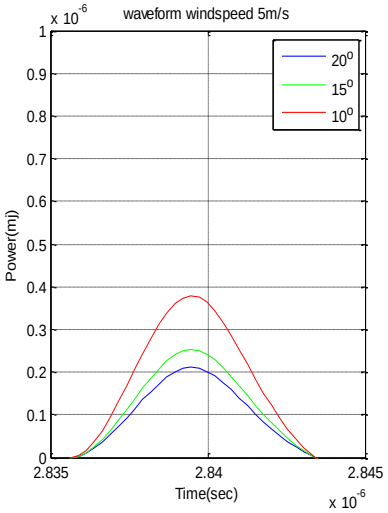

Figure 11. Low wind speed under different viewing angle's waveform

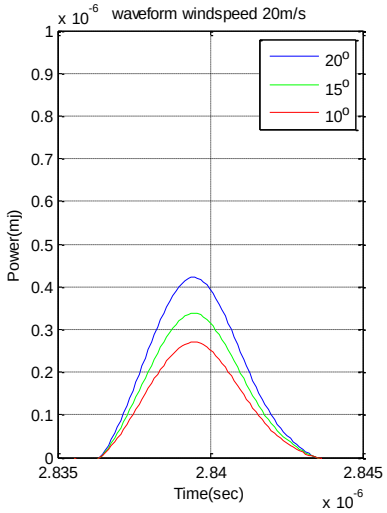

Figure 12. High wind speed under different viewing angle's waveform

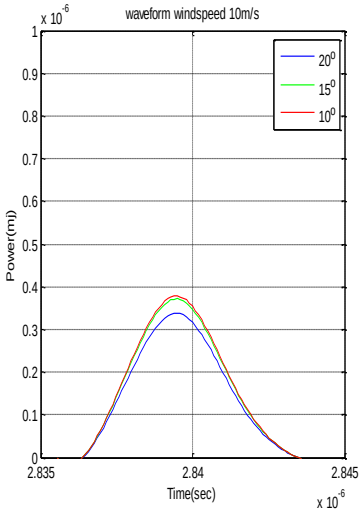

Figure 13. Middle wind speed under different viewing angle's waveform

4.2.3 Middle Wind Speed Figure 13 shows: waveforms under the case of wind speed 10m/s, viewing angle 10 and 15 are similar. Compared with Figure 11 and Figure 12, the differences of waveform amplitude among three different viewing angles are unapparent.

5. CONCLUSIONS

1. The research is based on wind-induced water surface model in order to simulate and analyze laser pulse's correlation to the water surface and its geometric and energy behavior. Furthermore, it is beneficial to the comprehension of ALB's detection of water surface and finding effective waveform data processing methods.
2. Low and middle wind speed are practical cases for meteorological conditions. Under viewing angle 20 degree, the appropriate timing estimator for low and middle wind speed is maximum slope change and 50% risetime point, respectively.

6. REFERENCES

Central Weather Bureau, site: http://www.cwb.gov.tw/V6/education/encyclopedia/me016.html (last access date: 2011/4/6).

Chu, C.J., 2011, hydrodynamics, site:http://www.cv.ncu.edu.tw/html/01_Intro/Faculty_Ch/Personal/THE01_index.htm (last access date: 2011/4/20)。

Meng, 2011, Simulation and Analysis of Airborne LiDAR Bathymetry on Capillary-Gravity Water Surface Detection, Master Thesis, Department of Civil Engineering, National Taiwan University.

Abshire, J. M., J.F. McGarray, L.K. Pacini, J.B. Blair, and C.G. Elman, 1994. Laser Altimetry Simulator version 3.0, User's Guide, NASA Technical Memorandum 104588, 66 p.

Law, A.M. and W.D. Kelton, 1991. Simulation Modeling and Analysis, McGraw-Hill, Inc., pp. 112-113 & 330.

Mobley, C.D., 2002. Light and Water: Radiative Transfer in Natural Waters, Academic Press, San Diego, CA, 592p.

Tulldahl, H.M. and K.O.Steinvall, 2004. Simulation of sea surface wave influence on small target detection with airborne laser depth sounding, Journal of Optical Society of America, 43, pp. 2462-2483.

Wang, C.K., W. Philpot, M. Kim, H.M. Lei, 2011. A Monte Carlo study of the seagrass-induced depth bias in bathymetric lidar, Journal of Optical Society of America, 19, pp. 7230-7243.